The smallest stroke: Occlusion of one penetrating vessel leads to infarction and a cognitive deficit

Andy Y. Shih[1], **Pablo Blinder**[1], **Philbert S. Tsai**[1], **Beth Friedman**[2], **Geoffrey Stanley**[1], **Patrick D. Lyden**[3], and **David Kleinfeld**[1,4]

[1]Department of Physics, University of California at San Diego, La Jolla, CA, USA

[2]Department of Pharmacology, University of California at San Diego, La Jolla, CA, USA

[3]Department of Neurology, Cedars-Sinai Hospital, Los Angeles, CA, USA

[4]Section of Neurobiology, University of California at San Diego, La Jolla, CA, USA

Abstract

Microinfarctions are present in the aged and injured human brain. Their clinical significance is controversial, with postulated sequelae ranging from cognitive sparing to vascular dementia. To address the consequences of microinfarcts, we used controlled optical methods to create occlusions of individual penetrating arterioles or venules within rat cortex. Single microinfarcts, targeted to encompass all or part of a cortical column, impaired performance in a macrovibrissa-based behavioral task. Further, multiple targeted vessels caused tissue damage that coalesced across cortex, even though the intervening penetrating vessels were acutely patent. Post-occlusion administration of Memantine, a glutamate receptor antagonist that reduces cognitive decline in Alzheimer's disease, ameliorated tissue damage and perceptual deficits. Collectively, these data imply that microinfarcts are likely contributors to cognitive decline. Strategies that have received limited success in the treatment of ischemic injury, which include therapeutics against excitotoxicity, may be successful against the progressive nature of vascular dementia.

Keywords

Excitotoxicity; ischemia; macrovibrissa; Memantine; NMDA receptor; somatosensation; two-photon microscopy; vasculature

---

Cognitive impairment as a consequence of age or injury has many root causes. An accumulation of evidence from aged patients suggests that a common basis for cognitive decline involves disruption of the microvasculature of the brain[1–3]. Post-mortem studies of patients with dementia have identified, in addition to other pathologies, an abundance of cortical microinfarcts[4–7] with diameters on the order of 0.1 to 1 mm (Fig. 1a). These microinfarcts are often juxtaposed to a variety of angiopathies, including hyaline arteriosclerosis, full and partially occluded vessel lumens, and inflamed vascular walls[4]. However, *in vivo* studies that seek to establish whether such microinfarcts occur concurrent

with cognitive decline, or are even predictive of decline, are hampered by an inability to resolve such small lesions with conventional non-invasive imaging[2]. Thus it is not clear if microinfarcts are largely benign or a contributing factor. This implies the need for an experimental model to directly examine the consequences of small vessel thrombosis in cortex and to serve as a test bed for treatments to mitigate cognitive impairment secondary to vascular disease.

The topology of rodent cortical angioarchitecture[8] has essential features that appear similar to that of humans[9]. This supports the utility of a rodent model to examine whether thrombosis of individual small cortical vessels could be the basis of microinfarction and whether strokes on such a small scale can negatively impact cognition. In this regard, we focus on penetrating vessels, the arterioles and venules that shuttle blood between the cortical surface and the parenchyma[10]. Past work shows that penetrating arterioles[11] and venules[12] form bottlenecks in the supply of blood to neighborhoods of microvessels. This highlights the penetrating vessel as a locus of vulnerability during vascular disease[8, 11, 12]. Loss of flow to even a single cortical penetrating arteriole will generate a nominally columnar microinfarction that can extend through the full depth of cortex[8, 13] (Fig. 1b). The small strokes in rodent appear to match human microinfarcts in geometry[14] (Fig. 1), and, as will be shown, the ability to induce a local inflammatory response, consistent with the correspondence in size between rodent and primate cortical microvessels[15, 16].

Here we address the potential cognitive impact of microinfarctions utilizing a rodent model of targeted micro-occlusions. Our overarching aim is to unravel the so-called "silent" features of microinfarcts in progressive cognitive decline, as well as to address their etiology and response to pharmacological intervention. We ask: (*i*) How is the extent of cortical microinfarction shaped by features such as vascular topology, blood volume flux, and the type of vessel? (*ii*) Can the occlusion of single cerebral vessel lead to cognitive impairment? (*iii*) How does the accumulation of multiple small vessel occlusions affect tissue integrity? (*iv*) What therapeutic agents may obviate the extent and potential impact of microinfarctions?

RESULTS

We used *in vivo* two-photon laser scanning microscopy[17] to visualize blood vessels and neurons through a cranial window in the somatosensory cortex of anesthetized rats[18]. Each cubic millimeter of rat cortex contains on average six penetrating arterioles and 16 penetrating venules (n = 9 rats). The penetrating vessels originate as branches from the surface vasculature and dive radially into the parenchyma (Fig. 2a). We categorized all vessels into three groups: penetrating arterioles, penetrating venules, and deep microvessels, *i.e.*, vascular segments that ramify from the penetrating vessel below the pial surface. Each type of vessel was found to be associated with a range of lumen diameters and red blood cell (RBC) velocities; these parameters were used to calculate volume flux through the vessel. Penetrating vessels supported values of flux[19] predominantly from 100 pL/s to 10 nL/s, while deep microvessels supported values primarily between 1 and 100 pL/s (Fig. 2b). The population of deep microvessels was further analyzed as vessel subtypes (Supplementary Fig. 1a–d), but was pooled here for clarity. We consider the tissue damage that results from occlusion of an individual vessel in each of these categories.

Our implementation of *in vivo* two-photon microscopy permitted us to form clots in targeted, individual blood vessels that lie both on and below the brain surface using two complementary techniques[20]. Penetrating vessels were occluded near the cortical surface by the linear absorption of focused green laser light in the presence of a circulating photosensitizer, Rose Bengal[21]. Occlusion of the vascular lumen was completed in 60 to 90

s. Deep microvessels were occluded by non-linear absorption of amplified, ultrashort laser pulses to generate highly focused irradiation without affecting tissue above or below the target vessel[22]. Occlusion of the microvascular lumen was complete within 120 s.

Acute consequences of single penetrating vessel occlusion

What is the time window for the onset of neuronal deficits? To answer this, we investigated the acute consequences of single penetrating vessel clots. We first used *in vivo* imaging of neuronal $[Ca^{2+}]$ by two-photon microscopy[17] to assess the loss of functionally evoked neuronal activity within the core of the microinfarct. For this, we imaged in the relatively large hindlimb region of the primary somatosensory cortex, where peripheral electrical stimulation could reliably activate a large number of neurons. The Ca^{2+}-sensitive dye OGB1-AM was loaded[23] intracortically, and the activity of layer 2/3 neurons in response to limb stimulation was quantified as a function of time after clot formation (Fig. 3a–e).

The number of neurons responsive to hindlimb stimulation was found to decrease precipitously within the first two hours after occlusion of a single penetrating arteriole (Fig. 3c). A similar effect was observed following occlusion of a single penetrating venule (Fig. 3d). As a control, Ca^{2+}-sensitive dye was also loaded into the region that represents forelimb, which lies more than one millimeter away from the hindlimb region. The forelimb area remained responsive to stimulation over a period of three hours, indicating that stroke-induced loss of function did not result from a general metabolic run-down of the animals (Fig. 3e). The occluded vessel was periodically monitored to ensure that the clot remained stable over the entire imaging period.

Consistent with loss of neural function in the core of the microinfarct, occlusion of either a penetrating arteriole or venule generated severely hypoxic conditions in the acute period of 6 hours post-occlusion, *i.e.,* pO_2 < 10 mm Hg, as reported by α-Hypoxyprobe™ staining in *post-hoc* histology[19] (Fig. 3f, **left panel**). The hypoxic tissue overlapped precisely with a column of severe vascular pathology in the microinfarct core (Fig. 3f, **right panel**), as highlighted by retention of the circulating fluorescein-dextran in the endothelia of the deep microvasculature[24]. Additionally, the microinfarct core exhibited increased labeling with α-3-nitrotyrosine, indicative of oxidative protein damage within cells and vasculature[25], as well as reduced α-aquaporin-4 staining and increased rat α-immunoglobulin G staining, indicative of pathology in astrocytes and blood brain barrier leakage[26], respectively (Supplementary Fig. 2). The border of the infarct was not spared from pathology, as it was delineated with propidium iodide-positive cells[27] (Fig. 3g); this is indicative of membrane degradation. We further noted reactivity with the macrophage marker α-CD68 both within and outside the core of the microinfarct (Fig. 3h). Staining for CD68 is a common marker for clinical microinfarcts[28]. Finally, a wall of microglial processes was observed along the stroke border, presumably as a response to limit the damage (Supplementary Fig. 3).

The finding that occlusion of a single penetrating vessel, whether arteriolar or venular, leads to multiple hallmarks of ischemic injury (Fig. 3f–h, Supplementary Figs. 2 & 3) is suggestive of an outward spread of cell death with a receding penumbra. In support of this hypothesis, waves of increasing intracellular $[Ca^{2+}]$ were observed to propagate outward from the core of the microinfarct across several hundred micrometers in response to penetrating arteriole occlusion, indicative of spreading depression[29] (Fig. 3i). The velocity of these events, *i.e.*, 30 to 70 μm/s, were similar to those seen in past *in vivo* imaging studies[30].

Microinfarction following single penetrating vessel clot

The occlusion of a single penetrating arteriole leads to a highly localized, nominally columnar region of tissue infarction over a course of seven days[8], as reproduced here and delineated by a region devoid of staining for the pan-neuronal marker α-NeuN in neuronal somata (Figs. 1b, 4a & Supplementary Fig. 4a), and by the local proliferation of reactive astrocytes (Fig. 1b & Supplementary Fig. 4a). The chronic result of occlusion to a penetrating venule is unreported and not readily predicted, as penetrating venules outnumber arterioles in rodent cortex and are highly collateralized on the pial surface[12]. Indeed, occlusion of a penetrating venule generated a microinfarction with remarkable similarity to that caused by occlusion of a penetrating arteriole, as seen with the loss of staining for α-NeuN (Fig. 4b & Supplementary Fig. 4b) and reactive astrogliosis (Supplementary Fig. 4b). Both microinfarct types exhibited dense packing of Nissl bodies, indicative of a gliotic, sub-acute lesion (Supplementary Fig. 4c,d). The penetrating arteriole and venule microinfarcts spanned, respectively, diameters of $460 \pm 70 \mu m$ (mean ± s.d.) and $500 \pm 120 \mu m$ and depths of 1.17 ± 0.32 mm and 1.30 ± 0.25 mm relative to the pia to yield the statistically identical microinfarct volumes of 220 ± 140 nL and 210 ± 100 nL. The volume of infarction is correlated with the pre-occlusion flux of RBCs through the vessel (Fig. 4d); occlusion of vessels with greater flux led to larger microinfarcts. These data show that there is an approximate equivalence, in terms of microinfarct generation, between occlusion of penetrating arterioles and venules.

In contrast to the case for penetrating vessels, the tissue infarction detected after occlusion of deep microvessels was minute (Fig. 4c,e). The targeted microvessels included direct branches of a source penetrating vessel or vessels that were two or more branch points distant to the penetrating vessel; endothelial retention of fluorescein-dextran served as a sensitive indicator of the targeted microvessel during histology[22]. We again assayed for small regions of necrotic damage using nuclear uptake of propidium iodide by dying cells[27]. We found that occlusion of those microvessels that were direct branches from the source penetrating vessel, *i.e.*, subsurface arterioles or venules, generated extremely small and transient regions of tissue damage, with a maximum infarct volume of 0.8 nL (Fig. 4e & Supplementary Fig. 1e). However occlusion of microvessels that were two or more branch points from the penetrating vessel, *i.e.*, capillaries, led to no detectable tissue damage (Fig. 4e & Supplementary Fig. 1f). These findings are consistent with a cyclically connected microvascular network, where flow in downstream vascular branches can reverse to compensate for loss of flow after clot formation[22]. Since occlusion of deep microvessels caused negligible damage in comparison with penetrating vessels, such lesions were not studied further.

Attenuation of microinfarct growth by NMDAR antagonists

We speculate that the acute expansion of the infarction, particularly as it involves excitotoxic waves (Fig. 3i), may be amenable to therapeutic intervention. Thus we next tested whether administration of neuroprotective agents after the onset of an infarction could mitigate its growth. Antagonists of NMDA-type glutamate receptors (NMDAR) are potential therapeutic agents for age-related pathologies thought to involve excitotoxicity, such as vascular dementia[31] and neurodegeneration[32]. We investigated the effect of a non-competitive glutamate receptor antagonist, MK-801, and a moderate-affinity uncompetitive glutamate receptor antagonist, Memantine, on microinfarct volumes caused by single penetrating vessel occlusions (Fig. 5a–c). Both antagonists, delivered by intraperitoneal injection, were found to be highly effective at reducing microinfarct volumes caused by occlusion of either a penetrating arteriole (Fig. 5d) or venule (Fig. 5e). Notably, Memantine was administered 30 to 45 minutes after the initiation of occlusions.

Summary statistics across all occlusions without and with NMDAR antagonists shows that the median radius of the infarct is reduced from 230 to 50 μm (Fig. 5f), which indicates a relatively large volume of salvageable penumbra. It is of interest that the maximum radius of the infarct, about 310 μm, is close to the distance from the occlusion where normal flow of RBCs within microvessels in layer 2/3 of cortex is reestablished (Fig. 5f). Further, the minimum radius of damage after treatment with either NMDAR antagonist, about 25 μm, corresponds to the radius for which blood flow was completely halted after a single, focal occlusion, *i.e.*, the ischemic core (Fig. 5f).

Cognitive deficit following penetrating vessel occlusion

We come to the crux of the issue and ask if the microinfarction that results from the occlusion of just one penetrating vessel generates a cognitive deficit. To address this question, we used a paradigm that involves somatosensation by macrovibrissa, the long hairs that rodents use to sense objects in front of them. The motion of each macrovibrissa is sensed by receptors whose outputs are conveyed predominantly to a single cortical column, roughly 400 μm in diameter, in primary vibrissa sensory (vS1) cortex[33, 34]. The task is based upon localized sensory input that leads to a cognitive decision and a motor plan, *i.e.*, to cross or not to cross, as opposed to a purely sensory measure.

Rats, with their mystacial pad trimmed down to one macrovibrissa, were trained to cross a gap that separated two elevated platforms for a reward of water[35]. The paradigm was operated in infrared light to remove sight as a potential confound. For relatively small gaps, a rat crossed the opening if the target platform could be contacted with the snout or paw (Fig. 6a). For intermediate gap distances, the rat perched at the edge of the platform and extended its macrovibrissa to sense the presence of the target platform before deciding whether to cross (Fig. 6b). Use of the macrovibrissa, rather than touching with the snout, allowed the rat to probe an additional distance, between one and two centimeters in practice, across the gap. Finally, as the gap was extended further, the rat was incapable of touching the target platform with the extended macrovibrissa and would not attempt to cross the gap lest it fall through the opening (Fig. 6c). This paradigm isolated the use of a single macrovibrissa to cross intermediate gap distances and thus provided readily controlled conditions to test a perception based on the functionality of the corresponding cortical column.

Once each animal was fully trained, we established a psychometric curve for the probability that the animal would cross a gap as a function of the width of the gap (Fig. 6d,f & h,j; **black curves**). This curve established the distance at which the animal had a 0.5-chance of crossing the gap and served as the baseline distance for subsequent comparison for the same animal.

The animals were divided into two cohorts. In the first cohort (n = 10; 4 arterioles and 6 venules) (Fig. 6d–g), identified as ON-target occlusion, vessels targeted for occlusion were selected using intrinsic optical imaging combined with vibrissa stimulation[36], in order to identify the location of the cortical column that received predominant input from the C1 or C2 macrovibrissa. We then occluded the penetrating vessel, arteriolar or venular, that was best centered in this column (Fig. 6e & Supplementary Fig. 5) and was expected to generate a microinfarct that encompassed the bulk of the superficial and middle layers of cortex (Fig. 4a,b). The animal was then re-assessed in the gap-crossing task on the fourth to seventh days post-occlusion (Fig. 6f; **red curve**). In each case, the animal could still perform the task when the gap was short enough for the animal to touch the target platform with its snout (Fig. 6f; **red circle**). However, with larger gaps the rat could no longer detect the target platform, even though videography showed that the target platform was contacted by the rat's macrovibrissa (Fig. 6f; **red square**). This behavioral deficit, from a single penetrating

vessel occlusion, was quantified in terms of a new psychometric curve, which showed that the navigable gap size decreased by about 1 cm for a 0.5-chance of crossing (Fig. 6f; *cf* **black & red curves**). Similar results were found across the cohort (Fig. 6g; **red bar**). Finally, as a positive control, removal of the single C1 or C2 macrovibrissa in the ON-target cohort resulted in a small, *i.e.*, ~ 0.1 cm, decrease in the navigable gap size for a 0.5-chance of crossing across the cohort (Fig. 6g; *cf* **red & blue bars**). This uncovered a small but significant functional compensation that is consistent with palpation that leads to activation of neighboring follicles, with their vibrissa stumps, and corresponding cortical columns[37].

In a second cohort of animals (n = 3), occlusions were made to penetrating vessels that supplied regions of cortex distant to the relevant cortical column in vS1 cortex (Fig. 6h–k), identified as OFF-target occlusions. These negative control animals showed no gap-crossing deficit caused by vascular occlusion (Fig. 6j; *cf* **black & red curves, red circle**). As a positive control for these animals, removal of the single macrovibrissa shifted the psychometric curve by over 1 cm, as expected since the animals could no longer touch the target platform (Fig. 6j; *cf* **red & blue curves, blue circle**). Similar results were found across the cohort of subjects (Fig. 6k).

Animals were euthanized on the last day of behavioral assessment to allow histological determination of the location and size of the infarct caused by penetrating vessel occlusion. These data showed that blockade of only a single penetrating vessel was sufficient to ablate an entire cortical column within the vS1 cortex of the ON-target group (Fig. 6e & Supplementary Fig. 5) and a similarly sized region outside of vS1 cortex for the OFF-target group (Fig. 6i & Supplementary Table 1). *In toto*, these data indicate that a strategically located microinfarct caused by occlusion of a single penetrating vessel will lead to a cognitive deficit.

Cognitive deficits are diminished by Memantine

The volume of microinfarcts secondary to occlusion of a penetrating vessel was substantially reduced by treatment with NMDA receptor antagonists (Fig. 5). We thus tested whether these therapeutic agents could provide an additional beneficial effect on reducing cognitive deficits secondary to an occlusion (Fig. 6). We made use of the gap-crossing task with ON-target occlusion (Fig. 6d–g), with the addition that Memantine was administered 30 to 45 minutes after the occlusion (Fig. 7a). The animals were then assessed in the task for an additional four to seven days post-occlusion. These animals, treated with Memantine, were able to cross essentially the same gap that was navigable prior to the occlusion (Fig. 7c,d). Removal of the remaining vibrissa as a positive control restored the full deficit in the example shown (Fig. 7c), and in general across the cohort (n = 7) (Fig. 7d & Supplementary Table 1).

The fraction of a cortical column that was impacted by a penetrating vessel occlusion depended upon the location and geometry of the microinfarct. The group of all ON-target data included microinfarcts roughly centered in the column; those with the administration of Memantine tended to be much smaller, and resultant microinfarcts often covered only a small fraction of the target column (Fig 7b & Supplementary Table 1). A plot of the perceptual deficit versus the measured fraction of the infarcted column is suggestive of a mid-point loss of function when only ~ 0.12 of the column is affected (Fig. 7e). This is reminiscent of a "mass action principle" for sparing of cortical function at the level of a single cortical column, in which the perception of the opposing platform across the gap is a monotonic function of the spared columnar volume[38]. Thus the extensive reduction in the perceptual deficit by post-occlusion administration of Memantine (Fig. 7f) is consistent with the concurrent reduction in the size of the microinfarct (Fig. 5f & Supplementary Table 1).

Coalescence of isolated microinfarcts

Larger infarcts often co-exist with microinfarcts in the human *post-mortem* brain tissue[4]. Could these have grown from a small set of initially isolated microinfarcts? To test this possibility, we occluded sets of well-separated arterioles and venules to form a multiplicity of microinfarcts in a region of cortex (Fig. 8). We observed that the resultant microinfarcts were likely to coalesce when the occlusions were spaced, on average, 1.6 mm or less apart; this corresponds to four to five penetrating vessels in the intervening space between occlusions (Fig. 8a,b,h). Further, occlusion of only 5.4 ± 1.1 % (mean ± s.d.) of the all of the penetrating vessels within an area of cortex led to complete infarction of the intervening tissue (n = 7) (Fig. 8b).

The basis of the coalescence of infarcts was revealed through longitudinal imaging studies on animals following occlusion of sets of penetrating vessels. Over a period of two days, these clots propagated beyond the initial core of the microinfarct to decrease the perfusion of neighboring penetrating vessels (Fig. 8c & Supplementary Fig. 6). Coalescence involved severe ischemic damage to the endothelial wall and eventual clot formation in the subsurface microvessels (Supplementary Fig. S7). Thus, the cortex appeared to be highly susceptible to sparse occlusion of penetrating vessels.

The finding that antagonists of NMDA receptors could decrease the volume of isolated microinfarcts (Fig. 5) suggests that the same therapeutic strategy may mitigate the coalescence of microinfarcts. To test this, we formed sets of well-separated single vessel occlusions, as above (Fig. 8a,b). The agent MK-801, delivered pre-occlusion, or the therapeutic Memantine, delivered post-occlusion, was injected intraperitoneally as described with isolated infarcts. We observed that both antagonists significantly reduced the total volume of infarcted tissue (Fig. 8d–g). Coalescence versus isolation of a microinfarct now became prevalent when occlusions were placed within 0.7 mm of each other (Fig. 8d,e,h), as opposed to the much larger distance of 1.6 mm in the absence of antagonists (Fig. 8a,b,h). Thus the minimum areal density for coalescence was increased by a factor of five through pharmacological intervention. Longitudinal imaging at the cortical surface of rats treated with MK-801 showed normal flow in surface vessels neighboring targeted vessels (Supplementary Fig. 8). Further, a subset of vessels originally occluded by photothrombosis were found to re-cannulate after one day, yet this was too late enough to prevent irreversible damage in the microinfarct core. *In toto*, these data show that therapeutic administration has a profound effect on not only the size of isolated microinfarcts, but also the coalescence of multiple microinfarcts (Fig. 8i).

DISCUSSION

The etiology and cognitive consequences of human cortical microinfarcts are unknown. To gain critical insight into this issue, we modeled microinfarct pathology (Fig. 1) through the selective occlusion of individual cortical penetrating arterioles and venules that supply blood to highly localized regions of tissue in the rodent cortex (Figs. 3 & 4). We found that microinfarcts were not innocuous, as has been often assumed from their small volume. Instead, the occlusion of only a single penetrating vessel leads to cognitive dysfunction in a behavioral task (Fig. 6). This implies that every cortical penetrating vessel can be critical for normal cognitive function. Further, we show that an accumulation of multiple microinfarcts leads to multiplicative tissue damage (Fig. 8), a novel mechanism of cortical injury that may result from small vessel disease. Critically, damage caused by both single and coalesced microinfarctions can be ameliorated with post-occlusion application of Memantine, a United States Federal Drug Administration-approved treatment for Alzheimer's disease and vascular dementia[39, 40] (Figs. 5 & 8). Consistent with the reduction in tissue damage, we observe a large improvement in cognitive function (Fig. 7).

The finding that microinfarcts could result from single penetrating venule occlusions was unexpected (Figs. 3 & 4), given their nearly three-to-one abundance compared to penetrating arterioles[12]. As with arterioles, there is limited collateral flow between penetrating venules[12], and each venule serves as a sink for the drainage of multiple neighboring penetrating arterioles[41], suggestive of a perfusion "domain". In human cortex, that ratio is reversed with penetrating arterioles outnumbering venules, indicating a larger venular perfusion domain that could be vulnerable to ischemia[42]. In contrast to arterial occlusion, venular thrombosis may involve additional mechanisms above ischemia, such as increased intracranial pressure and diapedesis of RBCs[43]. The contribution of venular pathology in dementia is unclear, as markers for vascular identification in *post-mortem* neuropathology are not commonly used. Venular collagenosis, which causes narrowing of the lumen, is a presumed source of poor cerebral blood flow in deep white matter, and has been described in vascular dementia[44]. Future efforts to distinguish between arterial and venular pathology in cortex would be of value, as venular collagenosis can be easily mistaken for more commonly observed hyalinized atherosclerosis.

We refined the gap-cross task to involve the use of a single macrovibrissa to sense a target platform (Fig. 6), as a means to ascertain the effect of a single microinfarct on cortical function. We found that the occlusion of a single penetrating arteriole was sufficient to disrupt the vibrissa column and abolish the processing of cortical input. This is a critical finding, since the behavioral significance of such small infarcts was previously unknown. This is consistent with the loss of somatosensory maps after small-scale stroke[45]. Indeed, the brain possesses remarkable plasticity and it is likely that, over time, the focal loss of cortical function in this task will be recovered through remapping of surrounding viable tissue[46, 47]. However, an issue of potential clinical importance is whether gradual accumulation of multiple microinfarcts becomes a source of long-term cognitive dysfunction. This possibility is supported by the profound alterations in the flow of neuronal electrical activity between separate cortical areas that occurs subsequent to the occlusion of a single cortical vessel[48].

The lack of flow after occlusion of a penetrating arteriole or venule and the death of nearby tissue (Fig. 4) implies that there is poor collateral flow among neighboring penetrating arterioles[11] and penetrating venules[12]. Nonetheless, an unexpected finding was the coalescence of individual microinfarctions into large cysts (Fig. 8b). This autocatalytic-like process can be induced by occlusion of only 5.4 % of the total penetrating vessels within a territory, with patent intervening vessels. Blood brain barrier breakdown is unlikely to contribute much to the coalescence effect, as microbleeds[49] and serum extravasation[45] cause surprisingly little neuronal damage. Rather, delayed thrombosis within the microvasculature may be involved, as recruitment of neighboring penetrating vessels into the ischemic zone occurs approximately 12 to 24 hours after the initial occlusions (Fig. 8c)

The potential occurrence of microinfarct coalescence in humans as a mechanism of accelerated brain injury remains to be addressed. In particular, we studied microinfarcts in subacute stages where astrogliosis and macrophage infiltration is prominent within the boundaries of the injury and tissue cavitation is incomplete. In later stages, the microinfarct is expected to become a fluid-filled cyst, which eventually collapses to become a linear scar or 'pucker' in chronic stages[3]. While the optically induced infarcts used in this work start on the surface of cortex, microinfarcts that are completely contained within the grey matter occur in humans[2]. Such subsurface microinfarcts could be formed in rodents with the use of amplified, ultrashort laser pulses to block flow in the deep part of a penetrating vessel[50]. High-field magnetic resonance imaging could shed light on the growth of microinfarcts and their correlation with the onset of cognitive decline. Further, different MRI sequences may be used to estimate the age of microinfarcts based on the sequelae of these changes[2].

The remarkable similarity of the vascular architecture and perfusion territory of human penetrating vessels with that of rodents leads to the conjecture that penetrating vessels are the locus of angiopathy leading to microinfarction in humans[9]. This highlights a need for animal models that accurately recapitulate the microvascular dysfunction, tissue pathology and behavioral consequences of vascular dementia. These models will act as test beds for pharmacological interventions, such as prophylactic slow-release anti-excitotoxic strategies, as well as for the development of contrast agents for noninvasive imaging of microinfarcts and longitudinal assessment of new drug treatments based on microinfarct growth. Lastly, it may be appropriate to re-evaluate past neuroprotective therapies to treat ischemic stroke, an abrupt illness, as a means to alleviate dementia, a slowly progressing disease.

Methods (Online)

Animal preparation

Two hundred and twenty male rats (Charles River), ranging in mass from 250 to 400 g and maintained in standard cages on a natural light-dark cycle, were used in this study. Eighty Sprague Dawley rats were involved in physiological and anatomical measurements, and 140 Long Evans rats were used for behavioral experiments, of which 20 of the 140 completed training to yield useful data. The care and experimental manipulation of our rats have been approved by the Institutional Animal Care and Use Committee at the University of California at San Diego.

All reagents were acquired from Sigma unless otherwise noted. Surgeries were performed under isoflurane (Baxter Healthcare) anesthesia, 4 % mean alveolar concentration (MAC) in 30 % oxygen and 70 % nitrous oxide for induction and 1 to 2 % MAC for maintenance. Body temperature was maintained at 37°C with a feedback-regulated heat pad (50-7053-F; Harvard). Heart rate and blood oxygen saturation were continuously monitored using a pulse oximeter (8600V; Nonin). Intraperitoneal injections of 5 % (w/v) glucose in 1 mL saline were given every 2 h for rehydration. Buprenorphine (0.02 mg/kg) was administered intraperitoneally for post-operative analgesia.

For acute studies (Figs. 2b & 3a–e,i), the femoral artery was cannulated for continuous measurement of blood pressure (BP1, World Precision Instruments) and withdrawal of blood for blood gas analysis (RapidLab 248; Bayer), and the femoral vein was similarly cannulated for delivery of reagents, *i.e.*, fluorescein-dextran, Rose Bengal and anesthetic. Prior to imaging, isoflurane was discontinued and anesthesia was transitioned to α-chloralose with an intravenous bolus injection of 50 mg/kg in saline, and then maintained with a steady flow of 40 mg/kg/h with a syringe pump. For survival studies (Figs. 1b, 3f–h, 4, 5 & 8), animals were maintained only on isoflurane for the duration of the surgery and imaging. In these cases, the femoral artery and vein were cannulated more distally to minimize disruption of blood flow in the leg. Since femoral artery catheters could affect locomotion, animals used in behavioral experiments, (Figs. 6 & 7), were catheterized only in the distal femoral vein for delivery of reagents.

Dura-removed cranial windows were generated over the somatosensory cortex, as described previously[20]. Cranial windows were centered on ±3 mm mediolateral and −0.5 mm anteroposterior for imaging of the hindlimb/forelimb sensory cortex, and +5.5 mm mediolateral and −3 mm anteroposterior for vS1.

Drug preparation and administration

The NMDAR antagonists MK-801 (Tocris) and Memantine (Tocris) were dissolved in sterile phosphate buffered saline (PBS) and stored at room temperature. MK-801 at a concentration of 1 mg/kg was administered 30 minutes prior to the initiation of vessel

occlusion, and Memantine at a concentration of 20 mg/kg was administered 30 minutes after initiation of occlusion. Both drugs were administered intraperitoneally. After drug administration, the animals were placed in a cage warmed to 32° C for 4 h to avoid possible hypothermia. Drug administration did not significantly alter the measured physiological variables (Supplementary Table 2).

Somatosensory cortex mapping

The sensory cortex was mapped by intrinsic optical imaging of blood de-oxygenation[51]. After craniotomy and durectomy, the exposed cortex was temporarily covered with agarose and a coverslip[20]. For identification of limb representations, the limb was electrically stimulated with a 0.5 to 1 mA, 10 ms pulse width, 3 Hz, 3 s train of pulses. For identification of barrel columns, single vibrissae were mechanically stimulated with a piezoelectric actuator under light isoflurane anesthesia. Images of a 3 × 3 mm area were acquired with a macroscope[52] fitted with a 12-bit CMOS camera (no. 1M60, Dalsa); the data were binned into 256 × 256 pixel frames at 2 frames per second for analysis. An initial image of the cortical surface vasculature made use of illumination by 475 nm center wavelength light emitting diodes (LEDs), which formed a reference to relate functional changes to specific locations within the window. Functional images were then obtained by illuminating the cortical surface with 630 nm center wavelength LEDs.

In vivo two-photon microscopy

Measurements of vascular structure, blood flow and intracellular $[Ca^{2+}]$ transients made use of a custom-designed two-photon laser-scanning microscope[53] with arbitrary scan patterns[54, 55] that further supported additional beams for linear[21] and nonlinear[22] thrombosis of single small vessels by focused lasers[56]. Control of scanning and data acquisition was achieved through the MPScope 2.0 software system[57]. The blood serum was labeled by intravenous injection of 0.3 mL of 2 MDa fluorescein-dextran (FD2000S; Sigma) prepared at a concentration of 5 % (w/v) in saline. Procedures for blood flow measurement and analysis have been described previously[20].

Calcium imaging—The membrane-permeant $[Ca^{2+}]$ indicator Oregon Green Bapta-AM (OGB1-AM; Invitrogen) was bolus-loaded into cortex as described previously[23]. Astrocytes were selectively labeled with sulforhodamine 101 (SR101)[58]. A 0.8-NA, 40-times magnification water-dipping objective was used for imaging. The excitation wavelength was 800 nm, and the collection band of OGB1 fluorescence was 350 to 570 nm and that of SR101 was 570 to 680 nm. Images were 400 by 256 pixels in size, and a time series consisted of 300 frames collected at 10 Hz. A single 0.5 to 1 mA, 10 ms pulse was applied to the hindlimb or forelimb to induce neuronal firing at frame 100 in each series. Data sets were collected once before occlusion and at various times post-occlusion. Each data set consisted of five different depths ranging from 200 to 400 μm below the surface (50 μm intervals), with five series collected at each depth. Mean arterial blood pressure, blood gases, and blood pH were maintained within normal physiological levels throughout the Ca^{2+} imaging and acute blood flow experiments.

Targeted occlusion of individual vessels—Penetrating vessels were occluded on the cortical surface by focal activation of the circulating photosensitizer, Rose Bengal, with a green laser (Crystalaser)[21]. Deep microvessels were occluded using an amplified 800 nm pulsed laser (Libra, Coherent)[22]. Technical and experimental details for both occlusion techniques have been described previously[56].

Immunohistology

Animals were perfusion fixed with 4 % (w/v) paraformaldehyde. The brain was post-fixed overnight at 4°C followed by equilibration with 30 % (w/v) sucrose. For most cases, the entire ipsilateral cortex was removed and sandwiched between two glass slides separated by a distance of 2.5 mm, prior to post-fixation. Brain sections, 50 μm in thickness, were then cut tangential to the cortical surface with a sliding microtome. Primary antibodies (Supplementary Table 3) were diluted in buffer that consisted of 10 % (v/v) goat serum (Vector Labs), 2 % (v/v) Triton X-100, and 0.2 % (w/v) sodium azide. Free-floating sections were then incubated overnight under slow rotation at room temperature in an antibody solution, washed in 50 mL of PBS for 30 minutes on an orbital shaker, incubated with secondary antibody (Supplementary Table 3) for 2 hours, washed again, mounted and dried on slides overnight. All slides were then sealed with Fluoromount-G (Southern Biotechnology Associates Inc.) and a No. 1 glass coverslip (Corning).

For pimonidazole hydrochloride (Hypoxyprobe™; Hypoxyprobe.com) immunostaining of hypoxic tissue[19], pimonidazole was injected through the femoral artery catheter one hour prior to perfusion fixation at a concentration of 60 mg/kg in a volume of 100 μL saline. For labeling of necrotic tissue, propidium iodide was injected intraperitoneally 2 hours prior to perfusion fixation, at a concentration of 1 mg/kg in a volume of 1 mL saline[27].

Macrovibrissa-dependent behavioral testing

The gap-cross apparatus consisted of two polyvinyl chloride platforms, shaped as isosceles trapezoids 20 cm wide in back, 10 cm wide in front, and 25 cm long, that faced each other on their short sides and were raised 50 cm above a table. The three non-opposing sides were enclosed with clear plastic and covered with a plastic roof to prevent the rats from exploring the other edges of the platform. Small wells were drilled into the far end of either platform and served as reward ports. Flow to each well was controlled by a solenoid which released 120 μL of water sweetened with 0.02 % (w/v) saccharin per spritz from a pressurized water bottle. Stepping motor controllers (no. UCC3055; Norberg) were installed at the base of each platform to allow the gap distance to be changed mechanically.

Rat centroid tracking—The platforms were located 30 cm in front of a flat black screen and illuminated by diffuse reflected light from two LEDs (M850 nm; ThorLabs). An infrared-sensitive CCD camera (no C3077-79; Hamamatsu) with a side view of the platform collected data at 60 frames per second. As the rat crossed back and forth between platforms for water rewards, its position was evaluated by computing the centroid of the image intensity. A crossing event was registered when the rat centroid crossed the gap and moved 2.5 cm beyond the edge of the target platform. The platform that the rat had crossed from was then repositioned to define a new gap distance; platforms were never repositioned while the rats were upon them. Occasionally, the rat would return back to the initial platform before the stages had fully repositioned. These crossings were flagged and omitted during post-processing. All computation and control made use of MATLAB™-based programs that processed the camera output, controlled the platform motors, and triggered the solenoids[59].

Macrovibrissa tracking—The macrovibrissae were imaged from overhead as the animals perched across the gap to palpate the target platform. We used a high-speed camera (Basler A602f) fitted with an f = 50 mm lens (Olympus f/1.2 Auto-S) located 80 cm above the platform. The camera was fixed to a separate stepping motor that was synchronized to move with the edge of the right platform. Frames were acquired 250 times per second. Two additional LEDs (M850 nm; ThorLabs) provided diffuse illumination of the gap region from below. The LEDs illuminated the flat-white interior of a 15 cm diameter by 10 cm long cylindrical tube with an aperture placed below the edge of the right platform.

Training Procedure—Rats were deprived of water 24 hours before their first run. As a first step, they were trained to run between the platforms in dim visible light with a bridge to fill the gap. Each successful cross would trigger the solenoid on the target platform to release a water reward. Rats that crossed 50-times or more their first day on the apparatus were kept as candidates for further training while the remainder were culled.

The successful animals were then trained to run between platforms separated by a small gap of 3 to 6 cm. Once they were comfortable crossing, the computer control was set to increase the gap width by an interval of 0.1 cm after every successful cross. Once they reached a gap they could not cross within a period of 120 s, the space would be reduced by several centimeters and the process would repeat. Using this "staircase" method, the rats were trained to cross increasingly larger gaps.

Once the rats were proficient at the staircase method, they were run in the same paradigm under infrared light, which was invisible to the rats. Initially, they were found to cross a gap only if the other platform was reachable with a front paw. With time, they gained the confidence to cross larger distances by stretching their upper torsos over the gap to touch the target platform with the snout. Finally, they learned to use their macrovibrissae to feel the edge of the target platform when it was past their snout, typically at a gap distance of 14 to 18 cm, which depended upon the size of the rat. Critically, training included randomly placed "blank" trials[35], where the gap distance was increased to a value larger than the rat could probe with its macrovibrissa. If the rat tried to jump the gap during such trials, it fell to a cushion on the table. This adverse experience assured that it would not jump without actively probing for the target platform in future trials. Falling during a blank trial was a necessary event for all trained rats, as it reinforced the need to palpate before crossing. *In toto*, approximately 30 % of the initial rats achieved this level of training.

Reducing the number of macrovibrissae to one—We found that animals trimmed to only a single macrovibrissa before the initial training failed to learn to use the macrovibrissa for the task. Thus, we allowed animals to learn the task with a full set of macrovibrissae, which were then sequentially trimmed. The first trim removed all macrovibrissae ipsilateral to the eventual microinfarct, the second trim removed the macrovibrissae in rows A and E on the contralateral side, the third trim removed the macrovibrissae in rows B and D, and the fourth trim removed all remaining macrovibrissae except C1 and C2. For the final trim, we used the high-speed macrovibrissa tracking data to determine which of the last two the animal was more reliant upon for gap-crossing, and trimmed the other. After each trim, the rat was run until its performance recovered to values achieved prior to trimming; this typically required one to three additional days of training. *In toto*, approximately 15 % of the initial rats achieved this level of training.

Psychometric testing program—After training, the animals were tested on the gap-crossing task using a probabilistic assessment of their abilities. Control software randomly selected one of five preset gap widths for each trial, which assured that the animal could not predict the next gap width. The highest width was set to one that the animal was not able to cross with its macrovibrissae because it was 1 cm out of reach, and the other four were successively 1 cm lower. The optimal range of gap distances for each animal was found empirically. Each run consisted of 80 to 120 trials, challenging the animal at least 15-times per gap distance. The number of successful crosses per gap distance returned a probability of crossing for each width (Fig. 6f). The deficit caused by a manipulation was calculated as the difference between curves at the 0.5-chance of crossing.

Pre-occlusion baseline—Three to four runs were used to establish a pre-occlusion baseline.

Post-occlusion data collection—Animals were given water *ad libitum* the night before surgery for vessel occlusion and for one day following surgery. Starting two days after the formation of an occlusion (Supplementary Fig. 5), the animals were run for an additional four to seven sessions to develop a post-occlusion baseline.

Macrovibrissa trim control—Once a stable post-occlusion baseline was established, the single remaining macrovibrissa was trimmed to its base. The animals were then run to establish a macrovibrissa-free baseline that served as a control.

All rats maintained ~90% of their original body weight over the duration of the study. They were run once every day, and were only given water from the apparatus.

Data analysis

Statistics—For the composite data in Figures 3c–e, 6g,k & 7d we used a repeated-measures ANOVA and a Tukey *post-hoc* analysis. For the composite data in Figures 5d,e, 7f & 8f,g we used the Kruskal Wallis test and a Dunn's *post hoc* analysis.

Infarct volume—To quantify microinfarct volumes we used α-NeuN stained tissue sections. Serial images of the microinfarct were collected at high-resolution with a stereoscope (MVX10; Olympus). The microinfarct boundary was delineated as the border between normal tissue exhibiting dense neuronal nuclei and infarcted regions devoid of nuclei (Supplementary Fig. 4a,b). Non-specific α-NeuN staining in the microinfarct core, likely due to undigested tissue matter, was easily distinguished from neuronal nuclei based on morphology. The area of tissue damage was measured in adjacent tissue sections and the total infarct volume, V_t, was calculated using the following formula: $V_t = (A_1 + A_2 + \ldots + A_n)h$, where A_n was the area of damage in the nth slice, and h was the distance between adjacent sections. With extremely small lesions caused by deep microvessel thrombosis, the damage was often limited to only a single slice (Fig. 4e and Supplementary Fig. 1e,f). In these cases, the volume of propidium iodide-positive tissue was measured with a confocal microscope, using a 1 μm step size (Olympus FV1000).

The volume of a barrel column was estimated as the area of the column at the level of layer 4, based on α-VGLUT2 staining (Figs. 6e,i, 7b & Supplementary Fig. 5h), times the thickness of cortex at that level of bregma, *i.e.,* 2.2 mm[60]. The area of the column was measured separately for each animal. For animals with the column completely infarcted, the area was estimated by averaging the area of two to three neighboring barrel columns that remained intact. Fractional damage (Fig. 7e) was computed by dividing the volume of infarcted tissue within the column by the total volume of the column. A mask of the column, derived at layer 4, was applied to all sections to delineate the column boundary through the depth of cortex. Deep penetrating vessels, identified as holes in a tangential slice, were used as fiducial markers for alignment of serial sections.

Calcium imaging analysis—Calcium indicator fluorescence from cell somata was extracted from planar image stacks using a supervised machine learning algorithm[54]. We excluded from analyses cells that were positively stained for SR101 in a second imaging channel, and fluorescein-dextran containing vessel segments. The $[Ca^{2+}]$ transients from individual neurons, indicative of action potential firing, exhibited an effectively instantaneous increase followed by an exponential decay over a 1 to 2 s period (Fig. 3b). We identified the onset of the transient by matched filtering with an idealized exponential decay, $e^{-(t-t_n)/\tau} \theta(t - t_n)$, where $\theta(t)$ is the Heaviside function, t_n is the putative event time and $\tau = 300$ ms. To be scored as a significant increase in $[Ca^{2+}]$ over baseline signal, the correlation between the data and the filter was required to be at least 2σ above zero, with σ defined

across a population of 1000 trace segments randomly collected from non-stimulation periods within the same data sets.

Supplementary Material

Refer to Web version on PubMed Central for supplementary material.

Acknowledgments

Abbreviations

NMDAR	*N*-methyl-D-aspartate type glutamate receptor
RBC	Red blood cell
s.d.	Standard deviation
s.e.m.	Standard error of the mean
vS1 cortex	Primary vibrissa sensory cortex

References

1. Gorelick PB, et al. Vascular contributions to cognitive impairment and dementia: A statement for healthcare professionals from the American Heart Association/American Stroke Association. Stroke. 2011; 42:2672–2713. [PubMed: 21778438]

2. Brundel M, de Bresser J, van Dillen JJ, Kappelle LJ, Biessels GJ. Cerebral microinfarcts: A systematic review of neuropathological studies. Journal of Cerebral Blood Flow & Metabolism. 2012; 32:425–436. [PubMed: 22234334]

3. Smith EE, Schneider JA, Wardlaw JM, Greenberg SM. Cerebral microinfarcts: The invisible lesions. Lancet Neurology. 2012; 11:272–282. [PubMed: 22341035]

4. Vinters HV, et al. Neuropathologic substrates of ischemic vascular dementia. Journal of Neuropathology and Experimental Neurology. 2000; 59:931–945. [PubMed: 11089571]

5. Kövari E, et al. Cortical microinfarcts and demyelination affect cognition in cases at high risk for dementia. Neurology. 2007; 66:927–931. [PubMed: 17372128]

6. Arvanitakis Z, Leurgans SE, Barnes LL, Bennett DA, Schneider JA. Microinfarct pathology, dementia, and cognitive systems. Stroke. 2010; 42:722–727. [PubMed: 21212395]

7. Jouvent E, et al. Intracortical infarcts in small vessel disease: A combined 7-T postmortem MRI and neuropathological case study in cerebral autosomal-dominant arteriopathy with subcortical infarcts and leukoencephalopthy. Stroke. 2011:e27–30. [PubMed: 21293025]

8. Blinder P, Shih AY, Rafie CA, Kleinfeld D. Topological basis for the robust distribution of blood to rodent neocortex. Proceedings of the National Academy of Sciences USA. 2010; 107:12670–12675.

9. Lauwers F, Cassot F, Lauwers-Cances V, Puwanarajah P, Duvernoy H. Morphometry of the human cerebral cortex microcirculation: General characteristics and space-related profiles. NeuroImage. 2008; 39:936–948. [PubMed: 17997329]

10. Bar T. The vascular system of the cerebral cortex. Advances in Anatomy, Embryology, and Cellular Biology. 1980; 59:1–62.

11. Nishimura N, Schaffer CB, Friedman B, Lyden PD, Kleinfeld D. Penetrating arterioles are a bottleneck in the perfusion of neocortex. Proceedings of the National Academy of Sciences USA. 2007; 104:365–370.

12. Nguyen J, Nishimura N, Fetcho RN, Iadecola C, Schaffer CB. Occlusion of cortical ascending venules causes blood flow decreases, reversals in flow direction, and vessel dilation in upstream capillaries. Journal of Cerebral Blood Flow & Metabolism. 2011; 31:2243–2254. [PubMed: 21712834]

13. Drew PJ, et al. Chronic optical access through a polished and reinforced thinned skull. Nature Methods. 2010; 7:981–984. [PubMed: 20966916]

14. Sofroniew MV, Vinters HV. Astrocytes: Biology and pathology. Acta Neuropathology. 2010; 119:7–35.

15. Tsai PS, et al. Correlations of neuronal and microvascular densities in murine cortex revealed by direct counting and colocalization of cell nuclei and microvessels. Journal of Neuroscience. 2009; 18:14553–14570. [PubMed: 19923289]

16. Weber B, Keller AL, Reichold J, Logothetis NK. The microvascular system of the striate and extrastriate visual cortex of the macaque. Cerebral Cortex. 2008; 18:2318–2330. [PubMed: 18222935]

17. Svoboda K, Denk W, Kleinfeld D, Tank DW. *In vivo* dendritic calcium dynamics in neocortical pyramidal neurons. Nature. 1997; 385:161–165. [PubMed: 8990119]

18. Kleinfeld D, Mitra PP, Helmchen F, Denk W. Fluctuations and stimulus-induced changes in blood flow observed in individual capillaries in layers 2 through 4 of rat neocortex. Proceedings of the National Academy of Sciences USA. 1998; 95:15741–15746.

19. Shih AY, et al. Active dilation of penetrating arterioles restores red blood cell flux to penumbral neocortex after focal stroke. Journal of Cerebral Blood Flow & Metabolism. 2009; 29:738–751. [PubMed: 19174826]

20. Shih AY, et al. Two-photon microscopy as a tool to study blood flow and neurovascular coupling in the rodent brain. Journal of Cerebral Blood Flow & Metabolism. 2012; 32:1277–1309. [PubMed: 22293983]

21. Schaffer CB, et al. Two-photon imaging of cortical surface microvessels reveals a robust redistribution in blood flow after vascular occlusion. Public Library of Science Biology. 2006; 4:258–270.

22. Nishimura N, et al. Targeted insult to individual subsurface cortical blood vessels using ultrashort laser pulses: Three models of stroke. Nature Methods. 2006; 3:99–108. [PubMed: 16432519]

23. Stosiek C, Garaschuk O, Holthoff K, Konnerth A. *In vivo* two-photon calcium imaging of neuronal networks. Proceedings of the National Academy of Sciences USA. 2003; 100:7319–7324.

24. Chen B, et al. Severe blood brain barrier disruption and surrounding tissue injury. Stroke. 2009; 40:666–674.

25. Calabrese V, Mancuso C, Calvani M, Rizzarelli E, Butterfield DA. Nitric oxide in the central nervous system: Neuroprotection versus neurotoxicity. Nature Reviews of Neuroscience. 2007; 8:766–775.

26. Friedman B, et al. Acute vascular disruption and Aquaporin 4 loss after stroke. Stroke. 2009; 40:2182–2190. [PubMed: 19372455]

27. Cevik IU, Dalkara T. Intravenously administered propidium iodide labels necrotic cells in the intact mouse brain after injury. Cell Death & Differentiation. 2003; 10:928–929. [PubMed: 12868000]

28. Soontornniyomkij V, et al. Cerebral microinfarcts associated with severe cerebral beta-amyloid angiopathy. Brain Pathology. 2010; 20:459–467. [PubMed: 19725828]

29. Siesjo BK, Bengtsson F. Calcium fluxes, calcium antagonists, and calcium-related pathology in brain ischemia, hypoglycemia, and spreading depression: A unifying hypothesis. Journal of Cerebral Blood Flow & Metabolism. 1989; 9:127–140. [PubMed: 2537841]

30. Murphy TH, Li P, Betts K, Liu R. Two-photon imaging of stroke onset *in vivo* reveals that NMDA-receptor independent ischemic depolarization is the major cause of rapid reversible damage to dendrites and spines. Journal of Neuroscience. 2008; 28:756–772.

31. Orgogozo JM, Rigaud AS, Stoffler A, Mobius HJ, Forette F. Efficacy and safety of Memantine in patients with mild to moderate vascular dementia. Stroke. 2002; 33:1834–1839. [PubMed: 12105362]

32. Olivares D, et al. N-Methyl D-Aspartate (NMDA) receptor antagonists and memantine treatment for Alzheimer's disease, vascular dementia and Parkinson's disease. Current Alzheimer Research. 2011; 9:746–758. [PubMed: 21875407]

33. Woolsey TA, Van Der Loos H. The structural organization of layer IV in the somatosensory region (SI) of mouse cerebral cortex. Brain Research. 1970; 17:205–242. [PubMed: 4904874]

34. Kleinfeld D, Deschênes M. Neuronal basis for object location in the vibrissa scanning sensorimotor system. Neuron. 2011; 72:455–468. [PubMed: 22078505]

35. Hutson KA, Masterton RB. The sensory contribution of a single vibrissa's cortical barrel. Journal of Neurophysiology. 1986; 56:1196–1223. [PubMed: 3783236]

36. Frostig RD, Dory Y, Kwon MC, Masino SA. Characterization of functional organization within rat barrel cortex using intrinsic signal optical imaging through a thinned skull. Proceedings of the National Academy of Sciences USA. 1993; 90:9998–10002.

37. Armstrong-James M, Fox K, Das-Gupta A. Flow of excitability within barrel cortex on striking a single vibrissa. Journal of Neurophysiology. 1992; 68:1345–1358. [PubMed: 1432088]

38. Lashley KS. Mass action in cerebral function. Science. 1932; 73:245–254. [PubMed: 17755301]

39. Reisberg B, et al. Memantine in moderate-to-severe Alzheimer's disease. New England Journal of Medicine. 2003; 348:1333–1341. [PubMed: 12672860]

40. Wilcock GK. Memantine for the treatment of dementia. Lancet Neurology. 2003; 2:503–505. [PubMed: 12878438]

41. Woolsey TA, et al. Neuronal units linked to microvascular modules in cerebral cortex: Response elements for imaging the brain. Cerebral Cortex. 1996; 6:647–660. [PubMed: 8921201]

42. Cassot F, et al. Branching patterns for arterioles and venules of the human cerebral cortex. Brain research. 2010; 1313:62–78. [PubMed: 20005216]

43. Villringer A, Mehraein S, Einhaupl KM. Pathophysiological aspects of cerebral sinus venous thrombosis. journal of Neuroradiology. 1994; 21:72–80.

44. Brown WR, Thore CR. Cerebral microvascular pathology in aging and neurodegeneration. Neuropathology and applied neurobiology. 2011; 37:56–74. [PubMed: 20946471]

45. Zhang S, Murphy TH. Imaging the impact of cortical microcirculation on synaptic structure and sensory-evoked hemodynamic responses *in vivo*. Public Library of Science Biology. 2007; 5:e119.

46. Troncoso E, et al. Recovery of evoked potentials, metabolic activity and behaviour in a mouse model of somatosensory cortex lesion: Role of the neural cell adhesion molecule (NCAM). Cerebral Cortex. 2004; 14:332–341. [PubMed: 14754871]

47. Carmichael ST. Plasticity of cortical projections after stroke. The Neuroscienist. 2003; 9:64–75.

48. Mohajerani MH, Aminoltejari K, Murphy TH. Targeted mini-strokes produce changes in interhemispheric sensory signal processing that are indicative of disinhibition within minutes. Proceedings of the National Academy of Sciences. 2011; 108:E183–E191.

49. Rosidi NL, et al. Cortical microhemorrhages cause local inflammation but do not trigger widespread dendrite degeneration. PLoS One. 2011; 6:e26612. [PubMed: 22028924]

50. Nishimura N, Rosidi NL, Iadecola C, Schaffer CB. Limitations of collateral flow after occlusion of a single cortical penetrating arteriole. Journal of Cerebral Blood Flow & Metabolism. 2010; 30:1914–1927. [PubMed: 20842163]

51. Frostig RD, Lieke EE, Ts'o DY, Grinvald A. Cortical functional architecture and local coupling between neuronal activity and the microcirculation revealed by *in vivo* high-resolution optical imaging of intrinsic signals. Proceedings of the National Academy of Sciences USA. 1990; 87:6082–6086.

52. Kleinfeld D, Delaney KR. Distributed representation of vibrissa movement in the upper layers of somatosensory cortex revealed with voltage sensitive dyes. Journal of Comparative Neurology. 1996; 375:89–108. [PubMed: 8913895]

53. Tsai, PS.; Kleinfeld, D. *In vivo* two-photon laser scanning microscopy with concurrent plasma-mediated ablation: Principles and hardware realization. In: Frostig, RD., editor. Methods for In Vivo Optical Imaging. 2. CRC Press; Boca Raton: 2009. p. 59-115.

54. Valmianski I, et al. Automatic identification of fluorescently labeled brain cells for rapid functional imaging. Journal of Neurophysiology. 2010; 104:1803–1811. [PubMed: 20610792]

55. Driscoll, JD.; Shih, AY.; Drew, PJ.; Cauwenberghs, G.; Kleinfeld, D. Two-photon imaging of blood flow in cortex. In: Helmchen, F.; Konnerth, A.; Yuste, R., editors. Imaging in Neuroscience: A Laboratory Manual. Cold Spring Harbor Laboratory Press; New York: 2011. p. 927-938.

56. Shih, AY., et al. Optically Induced Occlusion of Single Blood Vessels in Neocortex. In: Helmchen, F.; Konnerth, A.; Yuste, R., editors. Imaging in Neuroscience: A Laboratory Manual. Cold Spring Harbor Laboratory Press; New York: 2011. in press

57. Nguyen, Q-T.; Dolnick, EM.; Driscoll, J.; Kleinfeld, D. MPScope 2.0: A computer system for two-photon laser scanning microscopy with concurrent plasma-mediated ablation and electrophysiology. In: Frostig, RD., editor. Methods for In Vivo Optical Imaging. 2. CRC Press; Boca Raton: 2009. p. 117-142.

58. Nimmerjahn A, Kirchhoff F, Kerr JN, Helmchen F. Sulforhodamine 101 as a specific marker of astroglia in the neocortex *in vivo*. Nature Methods. 2004; 29:31–37. [PubMed: 15782150]

59. Mehta SB, Whitmer D, Figueroa R, Williams BA, Kleinfeld D. Active spatial perception in the vibrissa scanning sensorimotor system. Public Library of Science Biology. 2007; 5:309–322.

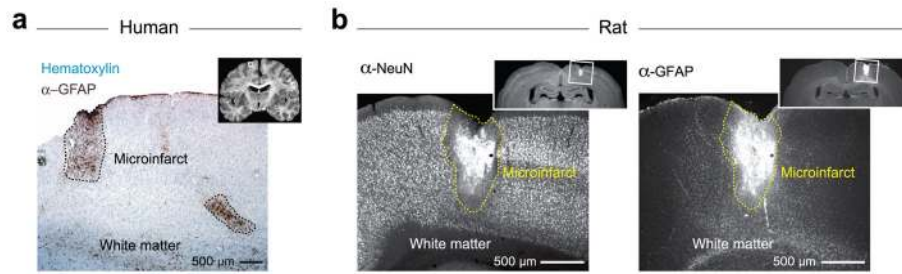60. Paxinos, G.; Watson, C. The Rat Brain in Stereotaxic Coordinates. Academic Press; San Diego: 1986.

Figure 1. Similarity between human and rat cortical microinfarcts
(a) Histology of microinfarcts detected in the cortex of an elderly human. The infarcted area is dense with reactive astrocytes that stain with glial fibrillary acidic protein (GFAP, brown). The tissue is counterstained with Hematoxylin (blue). Adapted from Sofroniew and Vinters[14]. **(b)** Microinfarct as seen 7 days after occlusion of a single penetrating arteriole in rat cortex. Neuronal viability is assessed with α-NeuN and astrogliosis is assessed with α-GFAP staining. Adapted from Blinder *et al.*[8].
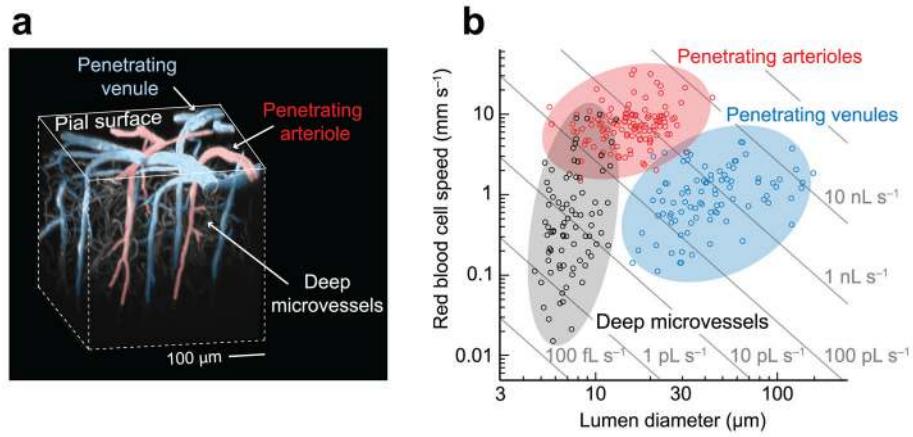
Figure 2. Topology and flow dynamics of cortical vasculature
(a) Three-dimensional reconstruction of cortical vasculature in a 0.5 mm^3 tissue volume collected from rat cortex *in vivo*. Penetrating arterioles (red) plunge into cortex to feed the deep microvasculature (white), while penetrating venules drain blood back toward the pial surface (blue). (b) Dynamics of RBC speed and lumen diameter collected from single vessels. The gray lines correspond to constant RBC volume flux.
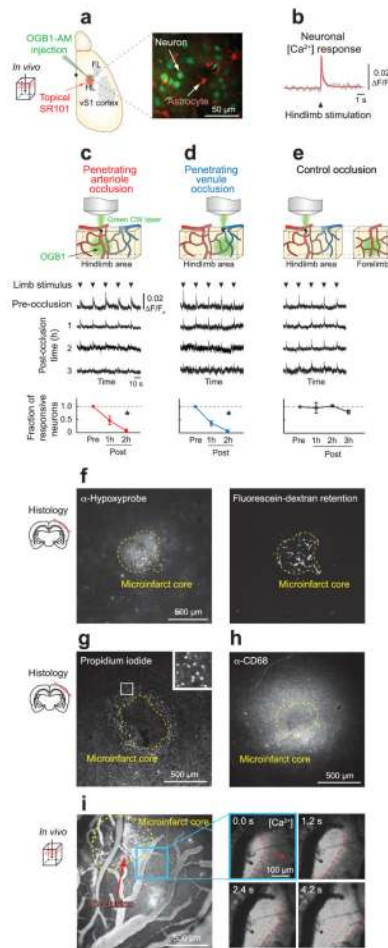
Figure 3. Acute neuropathology and growth of microinfarcts

(a) *In vivo* two-photon imaging of neuronal activity in the limb region of somatosensory cortex that was loaded with the Ca^{2+} indicator, OGB1-AM, and astrocyte-specific dye, SR101. **(b)** $[Ca^{2+}]$ responses from individual layer 2/3 neurons evoked by hindlimb stimulation. **(c)** Occlusion of a single penetrating arteriole is seen to gradually decrease responsiveness of local neurons. The lower panel shows the proportion of responsive neurons plotted as a function of time post-occlusion. Line graphs are presented as mean ± s.e.m. (n = 4; * p = 0.015, compared to baseline). **(d)** Occlusion of a single penetrating venule is seen to gradually decrease responsiveness of local neurons. The lower panel shows the proportion of responsive neurons over time. (n = 5; * p = 0.014, compared to baseline). **(e)** Distant control region within the same cranial window (forelimb), also loaded with OGB1-AM, shows no loss of neuronal responsiveness, following occlusion in hindlimb cortex (n = 4). **(f)** Histological examination of microinfarcts 6 hours post-occlusion. Tissue hypoxia, identified with α-Hypoxyprobe™ (n = 6 of each vessel type), overlaps with endothelial retention of fluorescein-dextran in the microinfarct core (yellow dotted line). **(g)** Ring of necrotic cells, as highlighted by propidium iodide uptake, delineate the microinfarct border (n = 4 of each vessel type). **(h)** α-CD68 staining of inflammatory cells (n = 11 of each vessel type). **(i)** Wave of cortical spreading depression, moving at 30 µm/s, observed by *in vivo* $[Ca^{2+}]$imaging (red dotted line) after occlusion of a single penetrating arteriole (red arrow in left panel). The Ca^{2+} wave was observed 30 minutes post-occlusion. The inset in the right panel (blue border), shows a time-course of magnified images.
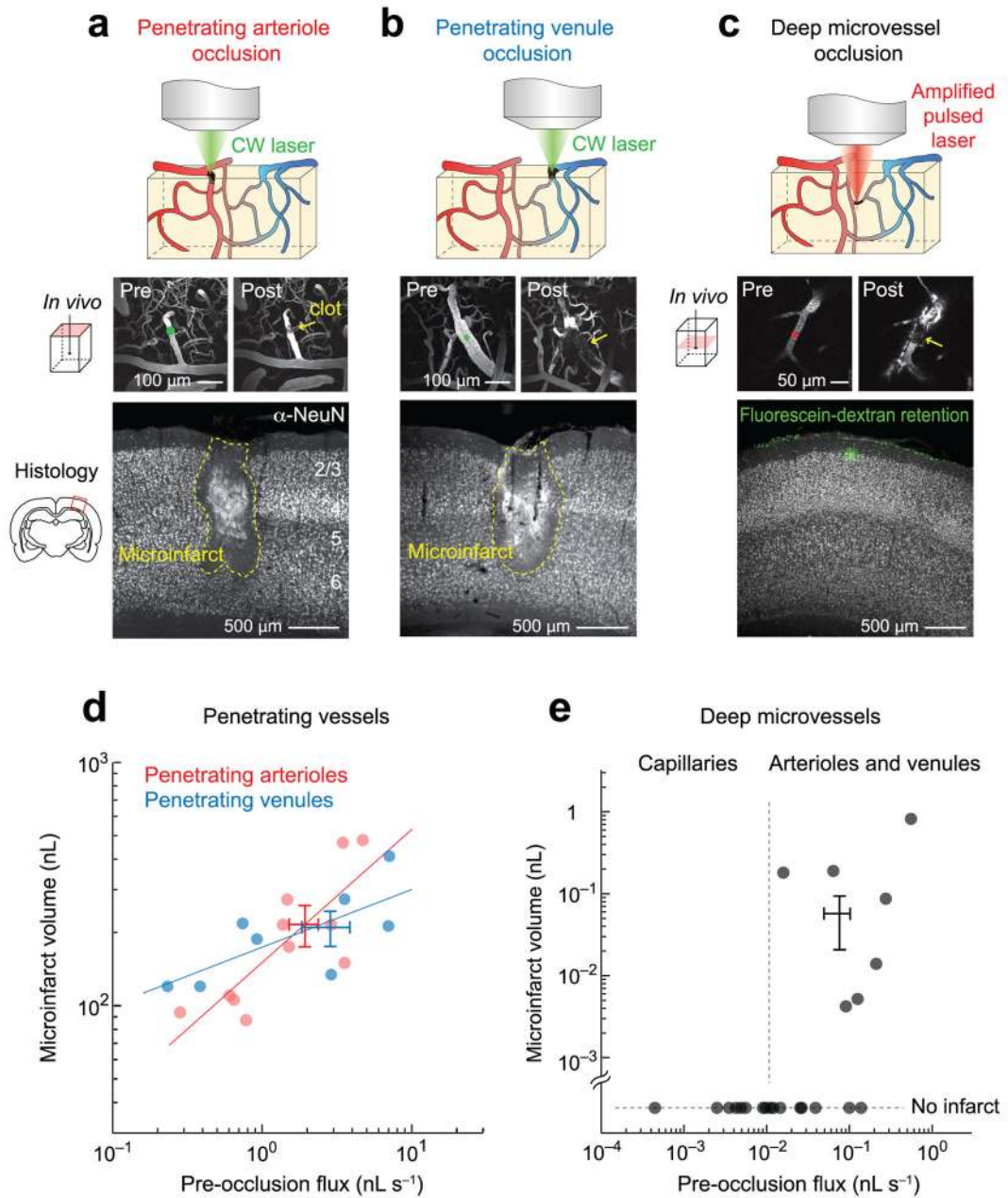
Figure 4. Chronic nature of microinfarcts caused by occlusion of penetrating arterioles and venules in rat cortex

(a to c) Microinfarcts that result from occlusion of single vessels. Each column shows a cartoon for the method of vascular occlusion (top), planar two-photon images of the target vessel before and after occlusion (middle), and assessment of tissue viability by α-NeuN immunohistochemistry 7 days post-occlusion. **(d)** Scatter plot of the microinfarct volume versus the pre-occlusion RBC volume flux of individual penetrating vessels. Microinfarct volume is correlated with flux; $R = 0.8$ ($n = 11$; $p = 0.0039$) for arterioles and $R = 0.7$ ($n = 8$; $p = 0.049$) for venules. The data follows a power law (fit lines) with volume $\propto$ (flux)^n, where $n = 0.33 \pm 0.05$ (mean slope $\pm$ s.d.) and 0.12 ± 0.02 for arterioles and venules, respectively. The crossbars show mean $\pm$ s.e.m for all data points in each vessel group. **(e)** Scatter plot of damage volume versus pre-occlusion RBC flux for individual deep

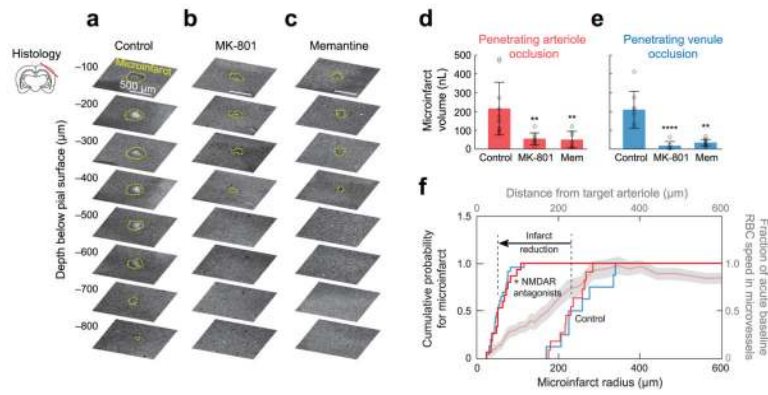microvessels. The crossbar shows mean ± s.e.m, excluding data points with microinfarct volumes of zero.

Figure 5. Reduction in the volume of isolated microinfarcts by administration of NMDAR antagonists

(a to c) Two NMDAR antagonists, MK-801 and Memantine (Mem), reduced microinfarct volume. Representative images of infarcted tissue, as assessed by α-NeuN immunohistochemistry, over a depth of 800 μm below the pial surface. **(d)** Volume of isolated microinfarcts that resulted from occlusion of individual penetrating arterioles in each treatment group. Bar graphs are presented as mean ± s.d. (n = 11, 8 and 7 for control, MK-801 and Memantine, respectively; ** p = 0.006 for control versus MK-801, and ** p = 0.003 for control versus Memantine). Pre-occlusion RBC volume fluxes of targeted vessels were not statistically different between groups (p = 0.44). **(e)** Volume of isolated infarct that resulted from occlusion of individual penetrating venules in each treatment group. (n = 8, 7 and 16 for control, MK-801 and Memantine, respectively; **** p < 0.0001 for control versus MK-801 and ** p = 0.002 for control versus Memantine). Pre-occlusion RBC fluxes of targeted vessels were not statistically different between groups (p = 0.51). **(f)** Cumulative probability of the radius of microinfarcts 5 to 7 days post-occlusion across all occlusion data with and without NMDAR antagonists. Red and blue curves correspond to penetration arterioles and venules, respectively. Note the strong reduction in size of the microinfarcts by treatment with antagonists. The muted curve is the acute decrease in the speed of RBCs in microvessels in layer 2/3 as a function of distance from the occlusion, adapted from Nishimura et al.[11]; data shown as mean (red) ± s.e.m (gray).
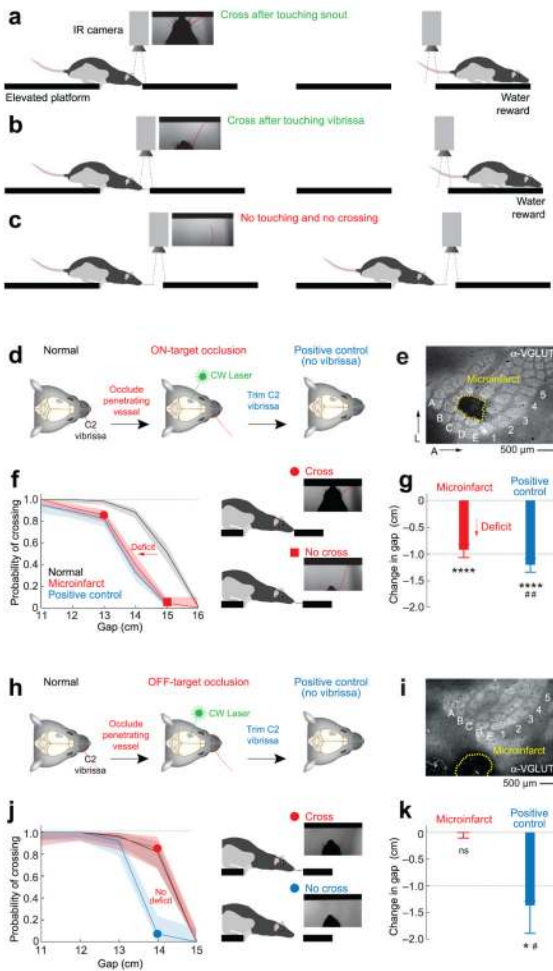
Figure 6. Cognitive deficit following single penetrating vessel occlusion in vibrissa primary sensory cortex

(a to c) Summary of rat behavior in gap-crossing task. At short distances, the animal detects the presence of the target platform with its snout (panel a). At intermediate distances, the animal extends its macrovibrissa to detect the platform (middle panel b). At long distances, the platform is not reachable and the animal does not cross (panel c). The images show vibrissa position in an attempt to contact the target platform during a single trial. **(d)** Experiment to test the effects of an ON-target stroke. **(e)** *Post hoc* histology shows a microinfarct localized to the C2 column after occlusion of a single penetrating venule. **(f)** Probability of successful crosses at each gap distance, with 0.95 confidence intervals, shown under normal conditions (black curve), following microinfarction (red curve), and following removal of the C2 macrovibrissa (blue curve). **(g)** Summary of gap-crossing deficits of the ON-target cohort. Bar graphs presented as mean ± s.e.m. (n = 10; **** p < 0.0001 compared to normal conditions, and ## p = 0.008, compared to post-microinfarct). **(h to k)** Control experiment to test the effects of an OFF-target stroke (n = 3; * p = 0.016, compared to normal conditions, and # p = 0.016, compared to post-microinfarct).
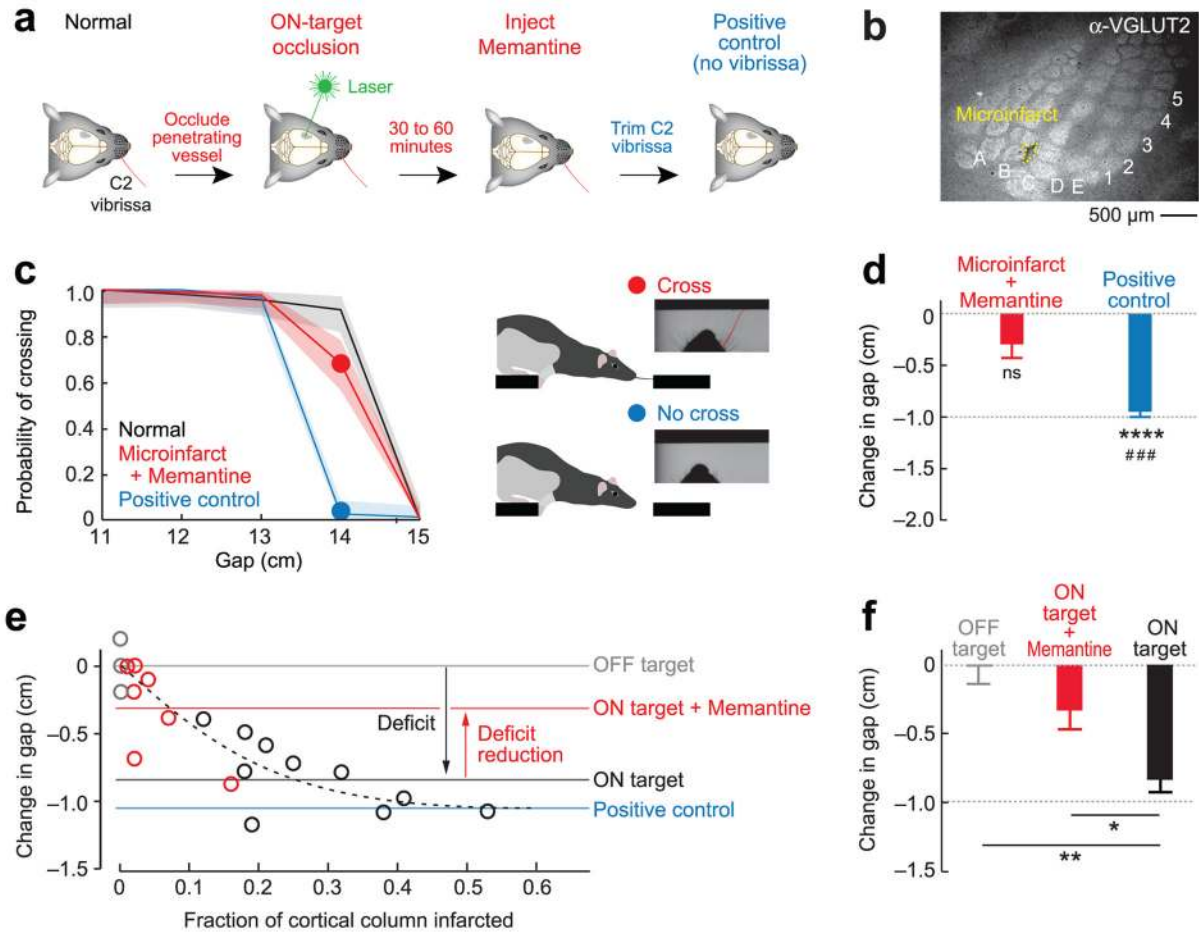
Figure 7. Reduction in cognitive deficit following single penetrating vessel occlusion by administration of the NMDAR antagonist Memantine

(a) Experiment to test the effects of an ON-target stroke followed by treatment with Memantine. **(b)** *Post hoc* immunohistochemistry shows a small microinfarct affecting part of the C2 column after occlusion of a single penetrating venule and treatment. **(c)** Probability of successful crosses at each gap distance, with 0.95 confidence intervals, shown under normal conditions (black curve), following microinfarction plus Memantine (red curve), and following removal of the C2 macrovibrissa (blue curve). Note that the animal is only slightly impaired. **(d)** Summary gap-cross deficits of the treated, ON-target cohort. Bar graphs presented as mean ± s.e.m (n = 7; **** p < 0.0001, compared to normal conditions, and ### p = 0.0006, compared to post-microinfarct; A non significant value of p = 0.1 was calculated for comparison of microinfarct plus Memantine with normal conditions). **(e)** Summary plot across all ON-target occlusion cases, Memantine-treated ON-target occlusion cases, and OFF-target control cases. Note the strong reduction in size of the behavioral deficit by the treatment with Memantine, consistent with a reduced fraction of cortical column infarcted. **(f)** Summary of the gap-cross deficits across all groups shows that the addition of Memantine leads to a significant reduction in the cognitive deficit for ON-target occlusion (n = 3, 7 and 10 for OFF-target, ON-target plus Memantine and ON-target, respectively; * p = 0.037, ** p = 0.009).
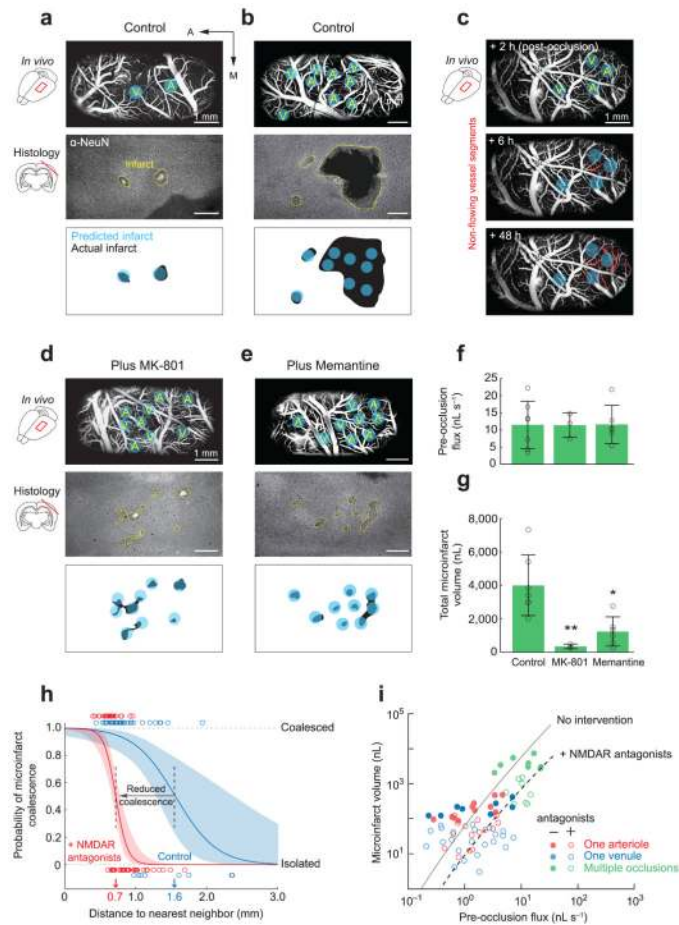
Figure 8. Potential coalescence of multiple, single penetrating vessel microinfarcts into an extended infarct

(a) Single penetrating vessel occlusions placed distantly from each other form isolated microinfarcts. Top panel shows wide-field view of vasculature as imaged by *in vivo* two-photon microscopy. The locations of occluded vessels are marked with a blue circle, with the area of the circle approximating the predicted microinfarct area, and a letter to indicate the target vessel type (A = one penetrating arteriole, V = one penetrating venule). Middle panel shows the actual microinfarct boundary at 7 days post-occlusion, as assessed by α-NeuN staining. Bottom panel shows predicted microinfarct regions overlaid with the actual microinfarct size. **(b)** Multiple penetrating vessel occlusions placed in close proximity coalesce into larger infarcts. **(c)** Gradual loss of flow in intervening penetrating vessels revealed by longitudinal imaging. Non-flowing vessel segments (red) are marked as a function of time on a planar image collected pre-occlusion. **(d and e)** Coalescence of microinfarcts is blocked by administration of MK-801 or Memantine. **(f)** Pre-occlusion RBC fluxes of targeted vessels were not statistically different between groups. Bar graphs presented as mean ± s.d. (n = 7, 3 and 6 for control, MK-801 and Memantine, respectively; p = 0.97). **(g)** Final microinfarct volumes were statistically different between groups (** p = 0.0054 and * p = 0.023, compared to control)**. (h)** The probability of coalescence in control and drug-treated groups as a function of distance from the nearest neighboring occluded vessel. The data is fitted with a logistic regression with 0.95 confidence intervals. **(i)** Hierarchy of microinfarcts sizes generated by single and multiple vessel occlusions with summary of the pharmacological effect of NMDAR blockers.